CHEMISTRY OF MATERIALS
ARTICLE
pubs.acs.org/cm

Ordered Large-Pore Mesoporous $Li_4Ti_5O_{12}$ Spinel Thin Film Electrodes with Nanocrystalline Framework for High Rate Rechargeable Lithium Batteries: Relationships among Charge Storage, Electrical Conductivity, and Nanoscale Structure

Jan Haetge, Pascal Hartmann, Kirstin Brezesinski, Juergen Janek, and Torsten Brezesinski*

Institute of Physical Chemistry, Justus-Liebig-University Giessen, Heinrich-Buff Ring 58, Giessen 35392, Germany

Supporting Information

ABSTRACT: Herein is reported the soft-templating synthesis and characterization of mesoporous lithium titanate ($Li_4Ti_5O_{12}$) thin film electrodes with a nanocrystalline framework. Various state-of-the-art techniques, including electron microscopy, grazing incidence small-angle X-ray scattering, impedance spectroscopy, time-of-flight secondary ion mass spectrometry, and X-ray photoelectron spectroscopy verify that the sol−gel derived $Li_4Ti_5O_{12}$ materials employed in this work are well-defined at both the nanoscale and the microscale. In addition, the data show that the thin films are highly crystalline after annealing in air at 650 °C and adopt the spinel structure in phase-pure form. The data also show that the conversion of the initially amorphous framework comes at little cost to the ordering of the distorted cubic network of pores averaging 18 nm in diameter. Apart from the structural characterization, we also examine the electrical conductivity and the charging/discharging behavior and show the benefits of producing a high quality material with mesoporous morphology. Mesoporous $Li_4Ti_5O_{12}$ thin film electrodes not only exhibit enhanced lithium ion storage capabilities at short charging times but also are able to maintain stable cycling performance at rates as high as 64C. We contend that the unique combination of open nanoscale porosity with electrical conductivity of the same order as that of ordinary bulk nanocrystalline $Li_4Ti_5O_{12}$ is responsible for the facile lithium intercalation observed in these thin film materials.

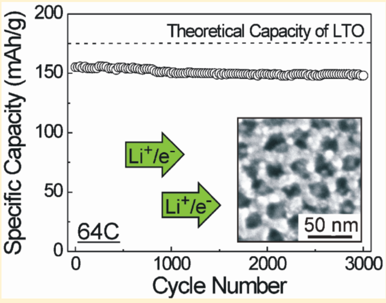

KEYWORDS: lithium titanate, LTO, mesoporous, self-assembly, anode, lithium ion battery, thin film

INTRODUCTION

Developments have clearly shown that nanocrystalline materials with open pore networks hold great promise for the fabrication of both next generation electrochemical capacitors[1] and intercalation electrodes for high rate rechargeable lithium batteries.[2−4] In particular, advances that receive widespread attention are those that broaden the scope of these materials by utilizing their unique combination of properties. Nanoporous redox active metal oxides with high surface area are particularly attractive for electrochemical energy storage applications, as there is the prospect of attaining greater power densities while maintaining energy density.[5,6] Such materials have several advantages over their traditional bulk counterparts. Apart from the short diffusion path lengths and pseudocapacitive contributions to charge storage,[7,8] it is known that the accommodation of lithium ions is associated with the expansion of the crystal lattice, and in bulk materials, the strain associated with partial Li^+ incorporation inhibits further intercalation.[9,10] For nanoporous materials, the enhanced charge storage capabilities are often due, in part, to the fact that they are able to freely expand upon lithiation.[3,11,12] This flexing of the pore network may relieve stress from volume expansion that normally inhibits charge storage, as shown for polymer-templated CeO_2 thin film electrodes.[11]

Among the existing redox active oxides that possess potential as intercalation electrodes for high rate rechargeable lithium batteries and asymmetric hybrid supercapacitors, $Li_4Ti_5O_{12}$ (LTO) plays an important role.[13−15] LTO belongs to the family of spinels within the solid solution regime of the Li/Ti/O ternary system. It is characterized by a cubic structure (space-group symmetry $Fd3m$) that possesses 56 atoms per unit cell, equivalent to eight formula units $Li[Li_{1/3}Ti_{5/3}]O_4$. In this structure, lithium atoms occupy all of the tetrahedral 8*a* and $^1/_6$ of the octahedral 16*d* sites. The remaining $^5/_6$ of the 16*d* sites are occupied by titanium atoms while the oxygen atoms forming a cubic-close-packed array are located at the 32*e* sites. Using the Wyckoff notation, the $Li_4Ti_5O_{12}$ spinel composition can be accurately written as $[Li_3]^{8a}[Li_1Ti_5]^{16d}[O_{12}]^{32e}$.

It has been shown that lithium can be reversibly intercalated into the spinel structure through a two-phase Faradaic reaction at a potential of approximately 1.55 V versus Li/Li^+. This reaction leads to a topotactic[16] transformation of LTO into rock-salt type $Li_7Ti_5O_{12}$. Eight lithium per unit cell can be intercalated. These lithium atoms occupy $^1/_2$ of the available octahedral 16*c* sites, while, at the same time, there is an internal displacement of the tetrahedrally coordinated lithium into the same 16*c* sites. We

Received: July 28, 2011
Published: September 16, 2011

note that the displacement of lithium ions is feasible as a result of the available interstitial space provided by the framework of the spinel structure. Overall, the fully lithiated phase can be accurately written as $[Li_6]^{16c}[Li_1Ti_5]^{16d}[O_{12}]^{32e}$.

One of the biggest advantages of LTO over other battery materials is that it does not undergo significant changes during lithiation. This means both that the lattice symmetry of the parent phase is unaltered and that the lattice expansion upon Li^+ intercalation is negligible. The latter is the reason why LTO is referred to as a zero-strain material.[15] Apart from the structural integrity and the fact that the charge/discharge curves exhibit a very flat voltage plateau, LTO materials also show excellent cycling stability.[17] In addition, it is important to note that LTO allows the lithiation to occur without the risk of dendrite growth due to Li plating.[18,19] The only major drawbacks are the relatively high potential versus lithium and the comparatively low theoretical capacity of 175 mAh/g. Overall, however, the aforementioned features make LTO very attractive as an anode material in both high rate rechargeable lithium batteries (in particular in combination with a high voltage cathode) and hybrid supercapacitors. The latter device architecture aims at combining the high energy density of redox active metal oxides with the high power density and long-term cycling stability of the materials employed in capacitive storage applications.[20,21] To this end, it has been shown that nanostructured LTO and activated carbon are highly suited for the fabrication of such hybrid supercapacitors.[13,21]

Polymer templating can be used to produce oxide materials with periodic nanoscale structures in the sub-40 nm size range.[22−25] The formation of these materials relies on the solution phase coassembly of inorganic building blocks with structure-directing agents.[26−29] The corresponding thin films can be achieved by the same coassembly methods but using an evaporation-induced self-assembly (EISA) process. This process was introduced by Brinker and Ogawa in the late 1990s and is still the method of choice for the direct synthesis of metal oxide thin films with nanoscale periodicity.[30,31] While several methods have been utilized to make LTO in forms other than bulk, including nanoparticles,[17,32] nanorods,[33] and nanofibers,[34,35] to our knowledge, the use of EISA to produce high quality mesoporous versions of this material has not yet been reported. This is due, in part, to the fact that the majority of the polymers used to template metal oxides do not allow the inorganic walls to be crystallized while retaining nanoscale porosity.

The present work focuses specifically on LTO spinel thin film electrodes, materials that we show here can be synthesized with both a well-defined mesoporous morphology and a nanocrystalline framework by utilizing a poly(ethylene-*co*-butylene)-*block*-poly(ethylene oxide) diblock copolymer, referred to as KLE,[36] as the structure-directing agent. We use these large-pore mesoporous materials as model systems for studying both electrical conductivity and charging behavior at short times in nanocrystalline LTO. By correlating electrical conductivity with redox activity, we are able to identify some of the unique advantages of using porous LTO architectures for high rate anode materials.

■ EXPERIMENTAL SECTION

Materials. Titanium(IV) *n*-butoxide (98%), anhydrous lithium acetate (99.99%), glacial acetic acid (99.99%), lithium perchlorate (battery grade, 99.99%), propylene carbonate (99.7%), ethanol, and 2-methoxyethanol were purchased from Sigma-Aldrich. $H[(CH_2CH_2)_{0.67}(CH_2CHCH_2CH_3)_{0.33}]_{89}(OCH_2CH_2)_{79}OH$, referred to as KLE,[36] was used as the structure-directing agent.

Synthesis. A mixture of 333 mg of $Ti(OBut)_4$ in 0.5 mL of dry EtOH and 0.15 mL of glacial acetic acid is combined with both 52 mg of $Li(CH_3COO)$ and 40 mg of KLE dissolved in 0.5 mL of dry ethanol and 1.0 mL of 2-methoxyethanol. Once the solution is homogeneous, thin films can be produced via dip-coating on polar substrates, including fluorine-doped SnO_2 (FTO) glass, (100)-oriented silicon wafers, and fused silica. Optimal conditions include relative humidities of 25−30% and constant withdrawal rates of 5−10 mm/s. For best results, the films are aged at 300 °C for 12 h and then calcined in air using a 35 min ramp to 650 °C followed by a 2 min soak.

Methods. Bright-field transmission electron microscopy (TEM) and scanning electron microscopy (SEM) images were taken with a CM30-ST microscope from Philips and a LEO GEMINI 982, respectively. Tapping mode atomic force microscopy (AFM) images were collected on a multimode atomic force microscope from Veeco Instruments, employing Olympus microcantilevers (resonance frequency, 300 kHz; force constant, 42 N/m). Wide-angle X-ray diffraction (WAXD) measurements were carried out on an X'Pert PRO diffractometer from PANalytical instruments. Grazing incidence small-angle X-ray scattering (GISAXS) patterns were collected at the German synchrotron radiation facility HASYLAB at DESY on beamline BW4, using a MarCCD area detector and a sample−detector distance of 1820 mm. X-ray photoelectron spectroscopy (XPS) spectra were acquired on a Physical Electronics ESCA 5600 spectrometer with monochromatic Al Kα X-ray source and a multichannel detector OmniIV. The electron takeoff angle to the sample surface was adjusted to 45°. The C 1s signal from adventitious hydrocarbon at 284.6 eV was used as the energy reference to correct for charging. The samples were also analyzed by time-of-flight secondary ion mass spectrometry (TOF-SIMS) using a TOF-SIMS 5 from ION-TOF GmbH. A primary ion beam of 25 keV Bi^+ was used to generate secondary ions for analysis. Sputter etching was carried out using a beam of 1 keV O^+ (I_0 = 131.1 nA). Krypton physisorption measurements were conducted at 87 K on 200 ± 10 nm thick LTO films with a total area of ~40 cm^2 using the Autosorb-1-MP automated gas adsorption station from Quantachrome Corporation. The film thickness was determined with an Alpha Step IQ Surface Profiler from KLA Tencor. For crystal structure visualization, the software Crystal Impact Diamond version 3.2g was used.

Electrochemical experiments were carried out in an argon filled JACOMEX glovebox (O_2 < 0.5 ppm; H_2O < 1 ppm) in a three-electrode cell using an Autolab PGSTAT302 potentiostat. A lithium foil several times the area of the working electrode was used as the counter electrode; the reference electrode was a lithium wire. The electrolyte solution was 1.0 mol/L $LiClO_4$ in propylene carbonate (PC). Cyclic voltammetry and galvanostatic charge/discharge measurements were conducted on LTO thin films to study the electrochemical behavior using cutoff voltages at 3.50 and 1.46 V (or 1.40 V) versus Li/Li^+. The loading of the films was 50 ± 2 μg/cm^2. The weight was calculated by directly measuring the thickness and porosity and knowing the density of the spinel phase.

Electrical conductivity measurements were conducted on 200 ± 10 nm thick LTO films on fused silica substrates using two interdigital Pt microelectrodes with an average electrode distance of 5 μm and an accumulated electrode length of ~900 mm on the top surface. Microelectrodes were produced via photolithography. First, a ~2 μm thick layer of a negative photoresist (ma-N 1420, micro resist technology GmbH) was deposited onto the LTO thin films and prebaked at 100 °C for 2 min. Structure transfer was done using a chrome-plated soda lime glass mask and a mask aligner (MA56, Karl Suss) with a UV broad band light source. After 85 s of light exposure at 365 nm (~6 mW/cm^2), the structure was developed using the ma-D 533s (micro resist technology GmbH) developer. Metallization was done by pulsed laser deposition using a Pt target, a KrF excimer laser at 248 nm, and an Ar background pressure of ~10^{-5} mbar. Liftoff was effected by dissolving the photoresist in acetone.

Complex impedance measurements were carried out using a Zahner IM6 electrochemical workstation with high impedance (HiZ) probe and ac amplitudes ranging between 100 and 500 mV. The obtained impedance spectra were fitted with the software ZSimpWin 3.21. Temperature-dependent measurements were done in a gastight tube furnace equipped with platinum wiring under continuous argon flow.

RESULTS AND DISCUSSION

The mesoporous LTO thin film materials were prepared by facile coassembly of molecular inorganic precursors with the large diblock copolymer KLE.[36] During the course of this work, we found that the use of titanium(IV) *n*-butoxide and anhydrous lithium acetate gives the best results in terms of pore ordering and phase purity.

To probe the mesoporous architectures, scanning electron microscopy (SEM), transmission electron microscopy (TEM), and atomic force microscopy (AFM) were used. The combination of these techniques allows imaging of both the top surface of the films and the porous interior. Figure 1 shows electron microscope and AFM images of mesoporous LTO thin films after removal of the KLE diblock copolymer and crystallization of the initially amorphous framework at 650 °C. Both the top view SEM and tapping mode AFM data reveal a distorted cubic network of open pores averaging 18 nm in diameter and further emphasize the homogeneity of the self-assembled samples. It is evident from these micrographs that the pore wall thickness is only slightly smaller than the mesopore cavities and that the nanocrystalline thin film materials employed in this work are crack-free at the micrometer level (see also Figure S1 in the Supporting Information). Moreover, AFM shows that the top surface is flat while the granular structure of the pore walls indicates the nanocrystalline nature of the KLE-templated LTO. From bright-field TEM and cross-sectional SEM, we are able to establish that the distorted cubic pore network persists throughout the bulk of the films. Figure 1g is an electron diffraction pattern collected from the same sample used for TEM imaging. The presence of Debye–Scherrer rings is typical of a material composed of nanocrystalline domains with random orientation. Calculated lattice spacings are in agreement with JCPDS (Joint

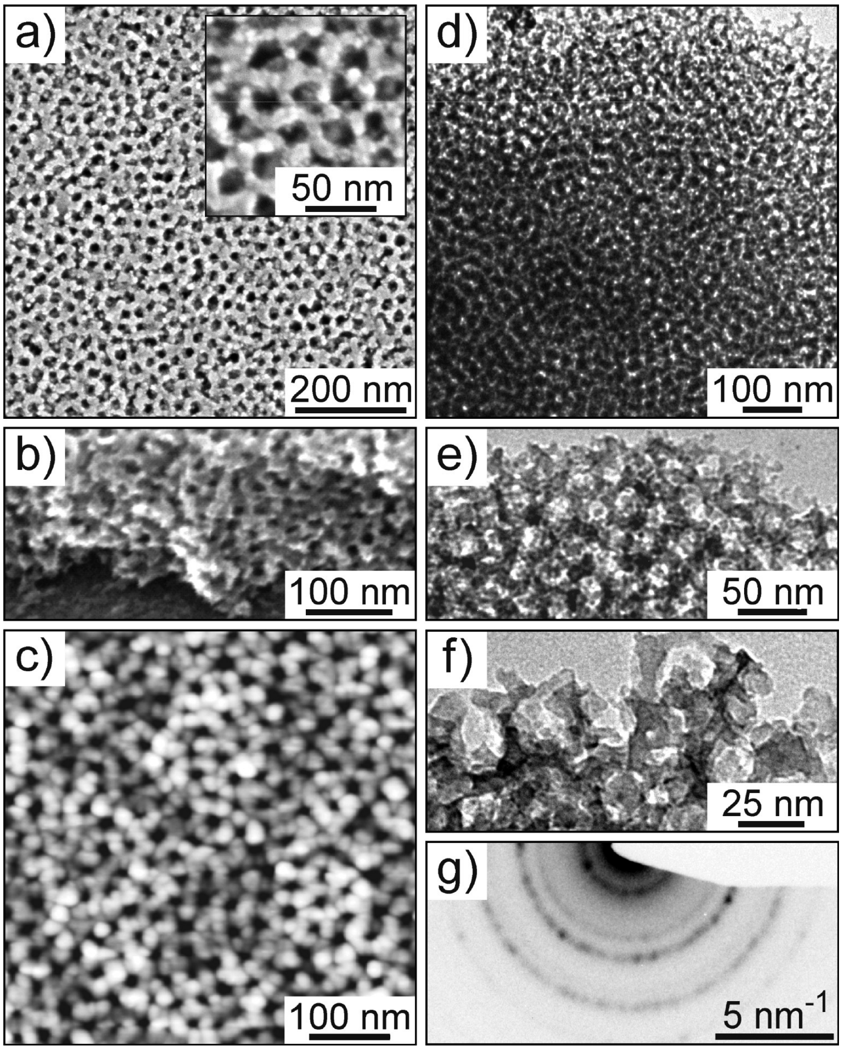

Figure 1. Morphology of KLE-templated LTO thin films calcined at 650 °C in air. (a) Top view SEM image showing open pores averaging 18 nm in diameter. A higher magnification SEM image is shown in the inset. (b) Cross-sectional SEM image. (c) Tapping mode AFM height image. The contrast covers height variations in the 1–7 nm range. (d–f) Low- and high-magnification bright-field TEM images showing that the distorted cubic pore structure observed at the top surface persists throughout the bulk of the films. (g) Selected area electron diffraction pattern showing Debye–Scherrer rings characteristic of cubic LTO.

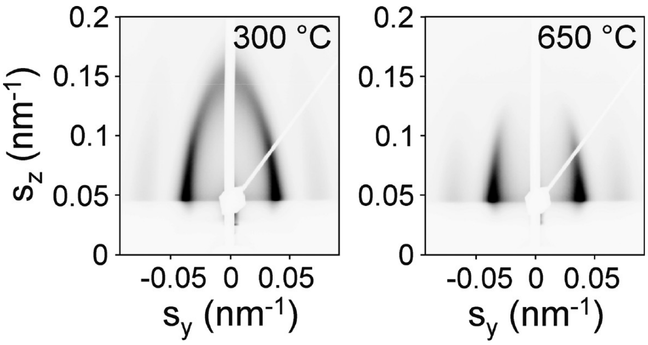

Figure 2. Synchrotron-based GISAXS on KLE-templated LTO thin films with both amorphous and nanocrystalline pore wall structures. Scattering patterns were collected at an angle of incidence $\beta = 0.2°$, and they show the evolution of the distorted cubic architecture upon thermal treatment. Scattering vector, **s**, components are given in nm^{-1}.

Committee on Powder Diffraction Standards) reference card no. 26-1198 for cubic LTO, thereby implying that the sol−gel derived materials adopt the spinel structure. Overall, the data in Figure 1 collectively verify that the KLE-templated thin films do not undergo severe restructuring; the mesoporous morphology is retained when the crystalline phase is achieved. We note that such restructurings are often observed for Pluronic-templated materials at the onset of crystallization as a result of the mismatch between critical nucleation size and pore wall thickness.[37]

These structure and morphology results are further supported by grazing incidence small-angle X-ray scattering (GISAXS) experiments. The scattering patterns shown in Figure 2 were collected at an angle of incidence, β, of 0.2° (defined as the angle between the X-ray beam and the plane of the substrate) on beamline BW4 at the Hamburger Synchrotronstrahlungslabor (HASYLAB) at Deutsches Elektronen-Synchrotron (DESY). Samples with amorphous framework produce distinct scattering maxima. These maxima are characteristic of a distorted cubic pore network with comparatively low preferred orientation relative to the substrate. However, the same GISAXS data also show second order reflections, thereby verifying reasonable in-plane and out-of-plane orders. Upon heating the samples to 650 °C to induce the conversion of the amorphous material to nanocrystalline LTO spinel, a loss of out-of-plane scattering is observed. The lack of strong scattering in the off-plane direction does not necessarily indicate a lack of out-of-plane order. Instead, it is due to both the small number of repeat units normal to the substrate and the process of crystallizing the inorganic framework itself, which may slightly disrupt the cubic pore structure. This hypothesis is supported by the fact that the in-plane scattering is still strong for samples calcined at 650 °C. Also, the presence of weak second order maxima provides ample evidence that the KLE-templated LTO materials can readily accommodate the spinel crystallites while retaining nanoscale porosity/periodicity and further suggests that they effectively withstand the stresses that develop during the course of thermal treatment.

We emphasize that the synthesis of materials that combine key features, such as well-defined nanoscale porosity, high crystallinity, and thermal stability, which are often a prerequisite for many applications, still constitutes a major challenge to current templating routes. The data in Figures 1 and 2 clearly show that the KLE-templated LTO samples meet all of these criteria. Thus, we think that they represent ideal model systems to study the charge storage properties of a material whose bulk form exhibits limited behavior.

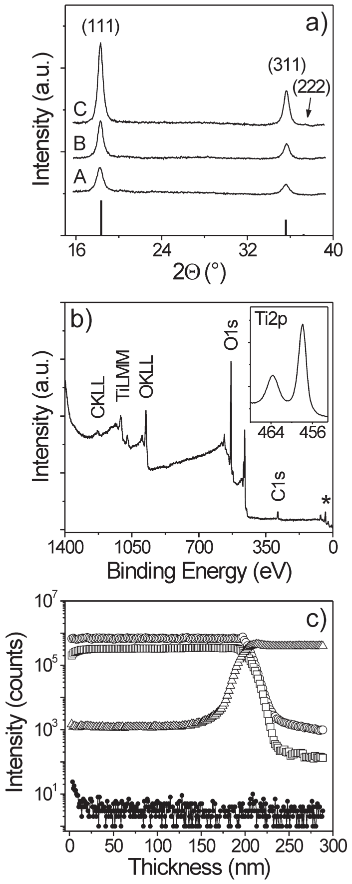

Figure 3. (a) WAXD data obtained on a KLE-templated LTO thin film calcined at (A) 600, (B) 625, and (C) 650 °C in air. The line pattern shows JCPDS reference card no. 26-1198 for cubic LTO. (b) Typical XPS survey spectrum. The Ti 3s, Li 1s, Ti 3p, and O 2s regions are indicated by an asterisk. A high-resolution spectrum of the Ti 2p core level is shown in the inset. (c) TOF-SIMS profile of a 200 nm thick LTO film on (100)-oriented silicon wafer showing the distribution of Li (○), Ti (□), Si (Δ), and C (●), as a function of depth from the top surface.

The elliptical shape of the GISAXS patterns in Figure 2 further indicates a large lattice contraction perpendicular to the plane of the substrate; the in-plane contraction is negligible as the materials are covalently bound to the substrate. A decrease in inorganic volume of about 75% is determined for films calcined at 300 °C. This volume change is associated with the formation of nonspherical pores, as shown in Figure 1b. At first glance, a unidirectional contraction of more than 70% seems rather large but is not in disagreement with other KLE-templated oxide materials made from molecular precursors.[8,11,38,39] Higher annealing temperatures do not lead to further contraction because the sol−gel derived LTO thin films are fully cross-linked by 300 °C.

Both Brunauer−Emmett−Teller (BET) surface area and porosity were determined by krypton physisorption measurements at 87 K. The use of krypton at 77 K was not appropriate to collect full adsorption/desorption isotherms, probably because of the gas−solid transition in the large mesopore cavities. Using a saturation pressure of 13 Torr (equivalent to 17.3 hPa) and a cross-sectional area of 20.5 Å for krypton, a BET surface area of 220 m^2/cm^3 and a porosity of 33% are obtained for LTO thin films calcined at 650 °C (we estimate the error margin to be ±5%). This result is typical of KLE-templated metal oxides in thin film format.

To more fully characterize the materials employed in this work, a series of wide-angle X-ray diffraction (WAXD), X-ray photoelectron spectroscopy (XPS), and time-of-flight secondary ion mass spectrometry (TOF-SIMS) measurements were carried out. These measurements provide insight into the crystallization behavior of the LTO thin films, their elemental composition, and whether second phases/impurities are present.

Figure 3a shows WAXD patterns obtained on a KLE-templated thin film calcined at 600, 625, and 650 °C in air. These data, along with the results from electron diffraction, establish that all characteristics of the self-assembled LTO materials can be associated with the desired spinel phase; neither pattern shows the presence of impurity phases, such as anatase or rutile TiO_2. The formation of such impurities is sometimes observed for LTO as a result of either phase separation or fluctuations in composition.[40] In this regard, it is important to note that the influence of small amounts of second phases upon the electrochemical properties is often underrated. The crystallization of the initially amorphous pore wall structure begins at temperatures of about 600 °C, which is in agreement with other LTO materials reported in the literature. Applying the Scherrer equation to the full width at half-maximum intensity of the (111) peak provides a crystallite size of approximately 11 nm. If this dimension is assumed to be the stable spinel domain size, it helps explain why the same synthesis using other block copolymers as the structure-directing agents, such as Pluronic F127 and P123, failed. The Scherrer analysis further indicates that the domain sizes of the crystallites are tunable from 11 to 15 nm. This result shows that the dimensions of both crystallites and structural confinement are almost of the same order after calcination at 650 °C. Moreover, it is also consistent with the electron microscopy data in Figure 1 and provides a hypothesis for understanding why the nanoscale porosity is fully retained. We emphasize that the KLE diblock copolymer produces cubic architectures with 25−35 nm repeat distances, which accommodate walls sufficiently thick to allow for uniform nucleation and growth of the crystalline phase.[11,38,39,41] In contrast, Pluronic type templates typically produce wall thicknesses closer to 5 nm.[42,43]

Figure 3b shows a typical XPS survey scan of KLE-templated LTO calcined at 650 °C in air. Aside from a weak C 1s peak, which we associate with adventitious hydrocarbon, only lithium, titanium, and oxygen core levels are observed. Figure 3b further shows a high resolution XPS spectrum of the Ti 2p region. This level consists of a single doublet due to spin orbit splitting with binding energies of 463.67 ± 0.05 eV and 457.98 ± 0.05 eV for the $p_{1/2}$ and $p_{3/2}$ lines, thereby indicating the presence of only Ti^{4+}. This result is not surprising, however, given that Ti^{4+} is the stable oxidation state under the experimental conditions. Lastly, we note that the Li/Ti stoichiometry could not be determined precisely because the Li 1s line at 54.06 ± 0.05 eV is partially obscured by an overlapping Ti 3p satellite peak (see Figure S2 in the Supporting Information).

The TOF-SIMS depth profile of a 200 nm thick mesoporous LTO film with a nanocrystalline framework on a (100)-oriented silicon wafer in Figure 3c illustrates the distribution of Li, Ti, Si, and C (as obtained from the corresponding secondary ions). It can be clearly seen from this data that both the metal ions are homogeneously distributed throughout the bulk of the films, which implies that larger fluctuations in composition can be ruled out and that the organic KLE template is fully removed. Only minor amounts of hydrocarbons can be detected at the top surface, which is in agreement with the XPS results in Figure 3b. The fact that the Si signal intensity begins to increase at a depth of about 160 nm is due to sputter induced ion mixing, which is typical of TOF-SIMS. Overall, the results with XPS and TOF-SIMS lead us to propose that the KLE-templated LTO thin films are well-defined not only at the nanoscale and microscale but also at the atomic level.

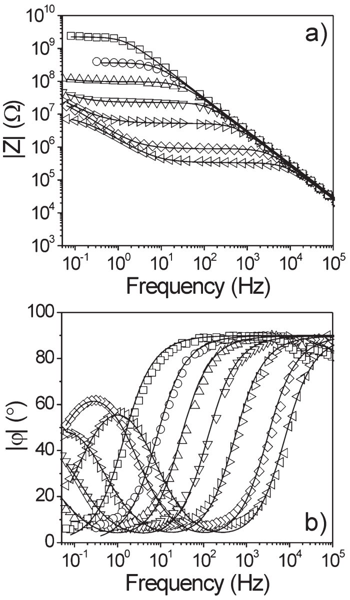

Figure 4. Complex impedance data collected on KLE-templated LTO thin films with a nanocrystalline pore wall structure at 320 (◁), 300 (◇), 242 (▷), 208 (▽), 179 (Δ), 150 (○), and 110 °C (□). Both the absolute value of impedance, |*Z*|, and phase angle, |*φ*|, as a function of frequency, *f*, are shown in parts a and b, respectively. Solid lines are fits to the experimental data. We note that outliers (due to interference with AC system voltage) that did not fit the overall trend of the data were removed.

Because the introduction of solid/solid and solid/gas interfaces into a material can dramatically alter the concentration and mobility of charge carriers, we also examined the electrical transport properties of the KLE-templated thin film materials. Bulk LTO is known for its rather poor electrical conductivity with predominant ionic contribution.[44] However, it has been shown that the electronic conductivity can be enhanced by either oxygen nonstoichiometry (reduction of Ti^{4+} to Ti^{3+}) or cation doping.[45]

The fast charge/discharge kinetics observed in the mesoporous LTO thin film electrodes employed in this work (see ensuing section on electrochemical charge storage) suggests that both the high density of grain boundaries due to the small domain sizes of the spinel crystallites and the large number of solid/air interfaces because of the nanoscale porosity have no profound effect on the electrical transport properties. To better understand this result, we measured the complex impedance which allows extracting of conductivity values. Figure 4 shows the total impedance and phase angle as a function of excitation frequency, *f*, for different temperatures and fits to the experimental data. All impedance spectra can be described using an

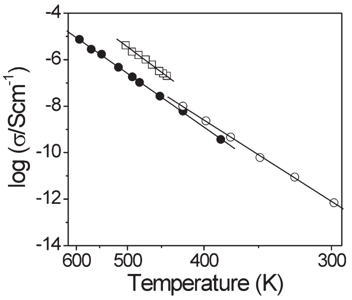

Figure 5. Arrhenius-type plot of the temperature-dependent electrical conductivity of KLE-templated LTO thin films (●) calcined at 650 °C. The activation energy for charge carrier transport is found to be equal to 0.96 eV. Reference data are shown for both nontemplated, nanocrystalline LTO (○) with an average crystallite size of 40 nm and commercially available material (□) with microcrystalline domain structure.[46,47]

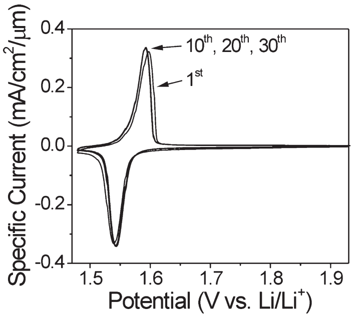

Figure 6. Voltammetry sweeps at a rate of 0.1 mV/s collected on a KLE-templated LTO thin film electrode with 15 nm diameter spinel domains. The 10th, 20th, and 30th cycles are superimposed.

equivalent circuit of two parallel resistor−capacitor (RC) circuits in series.

"High frequency" RC circuit: At maximum frequencies, the capacitor C_1 is indicated by the response with a slope of −1 for log(|Z|) versus log(f) and a phase close to −90°. The same impedance response is observed in all measurements, thereby implying that C_1 is nearly independent of the sample temperature. From the data in Figure 4, a value of 55 ± 6 pF is obtained for C_1. At lower frequencies, |Z| reaches a plateau while the phase changes to almost 0°. This result is characteristic of an ohmic resistance (R_1) contribution. R_1 is very sensitive to the sample temperature and varies from 3.4×10^5 Ω at 320 °C to 6.8×10^9 Ω at 110 °C. Measurements at lower temperatures could not be conducted on KLE-templated LTO thin films because the total impedance exceeded the range of our equipment.

"Low frequency" RC circuit: For measurements at higher temperatures, |Z| shows again a capacitive behavior (C_2) followed by an ohmic response (R_2) with very high impedance values, indicated by the increase of both |Z| and |φ| with decreasing f, followed by a plateau of |Z|. R_2 represents roughly the DC resistance of the sample. C_2 is a nonideal capacitor, as indicated by the slope smaller than −1. The best fits to the experimental data were obtained using a constant phase element (CPE) with an exponent equal to 0.85 (instead of 1 for ideal capacitor behavior). As a result of the limitations of the frequency range (100 mHz < f < 100 kHz), both R_2 and C_2 can only be determined at high temperatures, resulting in low maximum impedance values. The capacitive part of C_2 is found to be about 130 nF, with an uncertainty of 10−15%.

As mentioned above, LTO shows predominant lithium ion conductivity, and this fact helps explain the high values of R_2; the platinum microelectrodes block the mobile lithium ions at low frequencies. This in turn means that R_2 is associated with both the low electronic conductivity of the KLE-templated material and the charge transfer resistance across the Pt/LTO interface, while the capacity values for C_2 can be related to the double-layer at this interface. Because the contributions from charge transfer and electronic conductivity cannot be separated, the data shown in this work only provide information about the total conductivity (i.e., ionic and electronic). For a more detailed analysis of the electrical transport properties, it would be necessary to determine the transference numbers of the lithium ions and electrons, which is difficult to do for thin film materials with high impedance. Also, at elevated temperatures, lattice oxygen may contribute to the overall conductivity. At high frequencies, all mobile charge carriers follow the applied electric field. Thus, in the following, the R_1C_1 circuit is considered as the response of the mesoporous LTO thin films, and R_1 is used to calculate the total conductivity. However, a clear assignment of C_1 to a certain physical process cannot be made at this point, as a result of various possible capacitances (e.g., grain capacitance, substrate capacitance, etc.).

Figure 5 shows temperature-dependent conductivity data for KLE-templated LTO thin films in an Arrhenius-type plot. A comparison with data described in the literature shows that the mesoporous materials studied here exhibit a conductivity that is approximately 1 order of magnitude lower than that of microcrystalline samples but only slightly lower compared to nontemplated, nanocrystalline LTO.[44,46,47] We note that the data reported for these bulk materials were collected on pressed pellets rather than thin films. The total conductivity at room temperature can be estimated at 10^{-11} to 10^{-13} S/cm depending on the microstructure. Thinking in terms of battery applications, this result implies that efficient electronic wiring and short transport pathways are indispensable to achieve high charge/discharge rates without significant ohmic losses. Using the Arrhenius equation, we obtain an activation energy for charge carrier transport of 0.96 eV, which is consistent with reported measured values.[46,47]

In the above analysis, we treated the mesoporous LTO material as a bulk system and used the macroscopic geometry to examine the conductivity. This means that the nanoscale porosity was neglected even though the mesopore cavities do not contribute to charge transport. We are unaware of any suitable models that can be used for a more advanced analysis of the electrical conductivity of a mesoporous material with complex three-dimensional conduction pathways. However, it has been shown that the introduction of gas voids (ca. 30% by volume) into liquid electrolytes causes a reduction in conductivity by a factor of about 2.[48] With this in mind, the "effective" conductivity of our KLE-templated samples would be very similar to that of bulk nanocrystalline LTO.

To examine the redox processes present in KLE-templated LTO thin films, both solution-based cyclic voltammetry and galvanostatic charge/discharge experiments were conducted on samples calcined at 650 °C. As mentioned above, we are particularly interested in determining the charging behavior at short times because LTO nanomaterials are known to possess potential as intercalation electrodes for high rate rechargeable lithium batteries and hybrid supercapacitors.

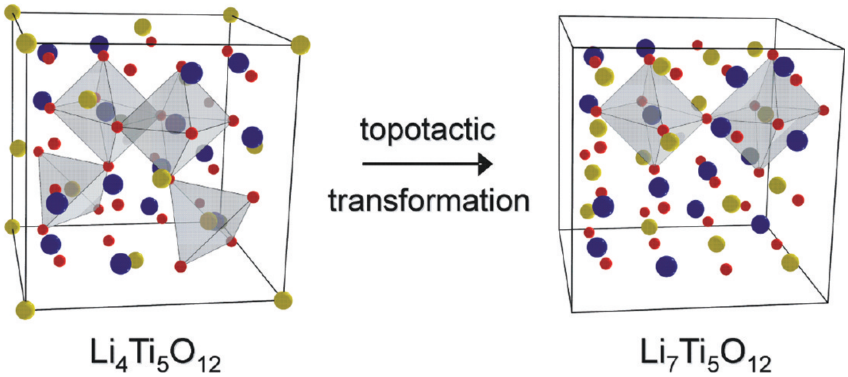

Figure 7. Scheme of the topotactic transformation of $[Li_3]^{8a}[Li_1Ti_5]^{16d}[O_{12}]^{32e}$ into $[Li_6]^{16c}[Li_1Ti_5]^{16d}[O_{12}]^{32e}$ upon lithiation. The unit cell of $Li_4Ti_5O_{12}$ spinel is shown on the left. Lithium atoms occupying the tetrahedral 8*a* sites are shown in yellow; lithium and titanium atoms on octahedral 16*d* sites are shown in blue; and oxygen atoms on 32*e* sites are shown in red. The unit cell of rock-salt type $Li_7Ti_5O_{12}$ is shown on the right. Eight lithium atoms per unit cell can be intercalated into the spinel structure. These lithium atoms occupy $^1/_2$ of the octahedral 16*c* sites; the tetrahedrally coordinated lithium atoms move to the same 16*c* sites. The different coordination spheres are indicated by gray polyhedra.

Initially, we chose cutoff voltages at 3.50 and 1.46 V versus Li/Li^+ because of concerns about the electrolyte stability. Figure 6 shows voltammetry sweeps collected at a rate of 0.1 mV/s, which reveal well-defined redox peaks. The cathodic peak at about 1.54 V can be attributed to the reversible intercalation of lithium ions into the spinel lattice through a two-phase Faradaic reaction. It has been shown that this reaction leads to a topotactic transformation of LTO into rock-salt type $Li_7Ti_5O_{12}$, as shown in Figure 7. From the data in Figure 6 we also conclude that the KLE-templated materials are, in fact, composed of purely cubic LTO and further exhibit excellent cycling behavior;[40] the total stored charge decreases only slightly between the 1st and 30th cycles.

Figure 8 shows the charge storage characteristics of mesoporous LTO thin film electrodes with a nanocrystalline framework. One surprising feature exhibited by these materials is the stable galvanostatic cycling performance at rates as high as 64C, with a specific capacity of initially more than 155 mAh/g. We note that 1C is defined as the intercalation of 1 Li^+ per formula unit in 1 h at 25 °C. Accordingly, this means that 1 Li^+ is intercalated in less than 1 min at a rate of 64C, which is very fast for a classical anode battery material.

Previous work has shown that the electrochemical properties of LTO, in particular the charge/discharge kinetics, can be significantly enhanced by reducing the size of the crystalline domains from microscale to nanoscale. For example, in 1998, Peramunage et al.[49] reported that micrometer-sized particles can be fully charged at rates of C/20−C/30, while nanoparticles can store the same mole fraction of lithium at approximately 1C.[17] The sluggish kinetics observed in microcrystalline LTO are due to the slow diffusion of Li^+ through the bulk of the material while nanoparticles provide for short diffusion path lengths for both electronic and lithium ion transport. Figure 8a shows that the KLE-templated samples are almost capable of reaching the theoretical capacity of 175 mAh/g at the 2C rate (in a narrower potential range than most previous reports), which demonstrates that the introduction of interconnected porosity, in fact, provides a beneficial microstructure for Li^+ insertion/extraction. The slight irreversibility on the first cycle might be associated with traces of water in the electrolyte. Thereafter, galvanostatic measurements indicate that mesoporous LTO can be reversibly cycled at 2C (170 mAh/g), 4C (168 mAh/g), 8C (165 mAh/g), 16C (162 mAh/g), and 32C (155 mAh/g) rates. The fact that the specific capacity varies with current density (or C-rate) emphasizes that kinetic limitations still have an impact on the

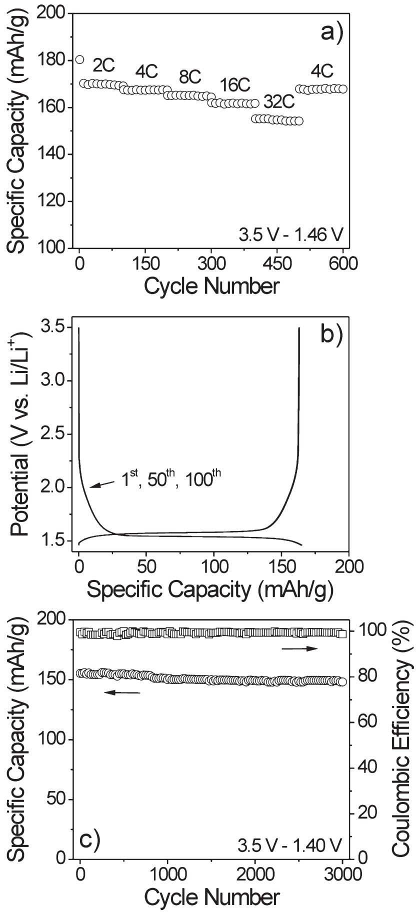

Figure 8. Charge storage characteristics of KLE-templated LTO thin film electrodes calcined at 650 °C. Cutoff voltages were set at 3.5 and 1.46 V in parts a and b and at 3.5 and 1.40 V vs Li/Li^+ in part c. (a) Specific capacity as a function of cycle number for various C-rates. (b) Galvanostatic charge/discharge curves obtained at a rate of 8C (23 $\mu A/cm^2$). The 1st, 50th, and 100th cycles are superimposed. (c) Specific capacity and Coulombic efficiency for the first 3000 cycles at a rate of 64C (184 $\mu A/cm^2$).

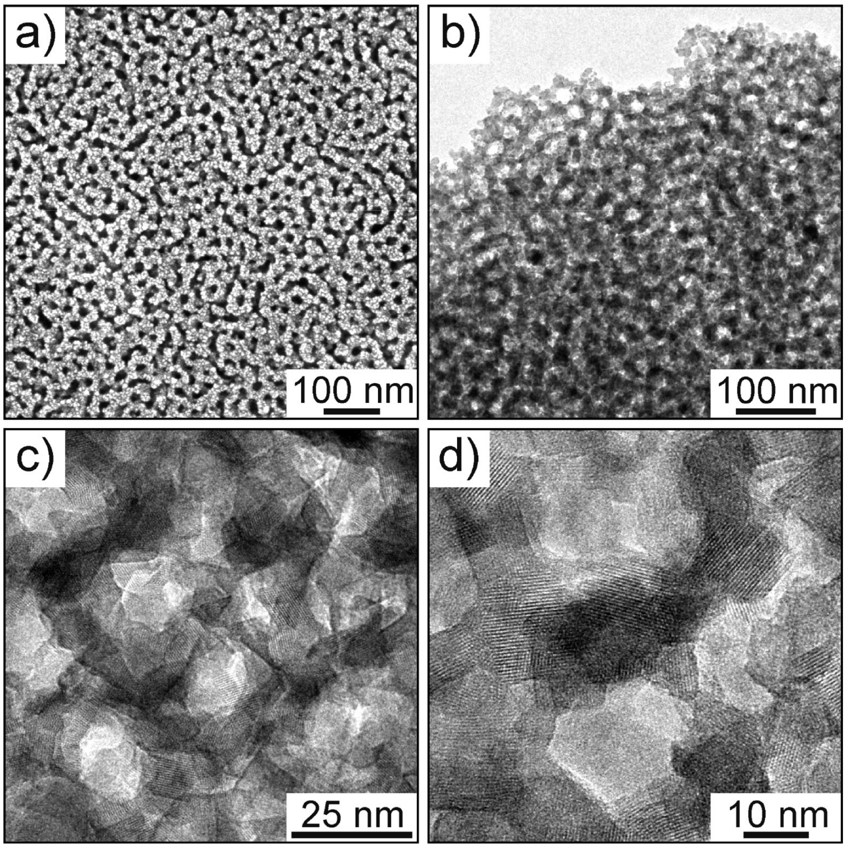

Figure 9. Morphology of a KLE-templated LTO thin film after galvanostatic cycling at a rate of 64C. (a) Top view SEM image. (b and c) Low- and high-magnification bright-field TEM images showing that the cubic network of open 18 nm diameter pores is retained after 3000 cycles. (d) HRTEM image from the same sample.

electrochemical performance of LTO—despite the optimized microstructure. We note, however, that the variation is less strong compared to most of the LTO materials reported in the literature. Two factors are expected to be responsible for the facile lithium intercalation observed in KLE-templated thin film electrodes. The total conductivity is very similar to that of bulk nanocrystalline LTO despite the larger number of interfaces, as a result of both the nanoscale porosity and the small domain sizes of the spinel crystallites. Perhaps more important, however, because the films employed in this work are fairly thin (~200 nm), is the nanoscale porosity, which allows the electrolyte to freely access the entire material volume and exposes the edges of the nanocrystalline domains in the pore walls for facile Li^+ insertion. This unique combination of factors is likely responsible for the fast insertion/extraction kinetics.

Figure 8b shows the galvanostatic charge/discharge curves obtained at a rate of 8C. These curves underline the highly reversible nature of the topotactic reaction between Li^+ and nanocrystalline LTO with Coulombic efficiencies close to 100%. A closer examination of Figure 8b reveals the sloping behavior of the discharge curves before the constant voltage plateau region is reached at about 1.53 V versus Li/Li^+. This linear behavior is characteristic of a capacitive discharge.

In recent years, it has been shown that pseudocapacitive effects[7,8,50] (i.e., charge is stored through Faradaic charge-transfer reactions with surface atoms) rather than double-layer processes[51] (i.e., charge is stored electrostatically in a thin double-layer at the electrode/electrolyte interface) play an important role in the performance of mesoporous metal oxide thin films. Part of the reason for this is the fact that the electrochemical properties of such materials are determined by surfaces and interfaces and not by bulk behavior only. For LTO, however, these charge storage processes play a minor role, as can be seen in Figure 8b.

From the data in Figure 8a, it is also apparent that the mesoporous LTO thin film electrodes experience a larger decrease in capacity between the 16C and 32C rates. This drop can be attributed to a shift of the constant voltage plateau region toward the lower potential, as a result of ohmic losses. For this reason, we decided to change the lower cutoff voltage from 1.46 to 1.40 V versus Li/Li^+ for the even higher C-rates. Figure 8c shows both the specific capacity and Coulombic efficiency at 64C. It can clearly be seen that the KLE-templated materials exhibit excellent reversibility. The capacity decreases from 155 to 148 mAh/g between the 1st and 3000th cycles, which is equivalent to a capacity fade of only 1.5×10^{-3} % per cycle. Also, the Coulombic efficiency stabilizes above 99% after the first few cycles. These results demonstrate that the LTO thin film electrodes are able to maintain stable cycling performance at rates as high as 64C.

Lastly, Figure 9 shows SEM and TEM images, which were collected on the same sample used for galvanostatic experiments at the 64C rate to determine whether structural changes occur upon lithiation. These images provide ample evidence that galvanostatic cycling, even at such high C-rates, leads neither to severe restructuring of the distorted cubic pore network nor to the appearance of cracks at the micrometer level (see also Figure

S1 in the Supporting Information), which helps explain both the excellent cycling stability and rate capability of these thin film materials. In addition, the high-resolution TEM (HRTEM) image indicates that the samples do not undergo amorphization or nanocrystalline domain growth.

Overall, the data clearly show that open nanoscale porosity can significantly enhance the lithium ion storage capabilities of nanocrystalline LTO at short charging times regardless of the poor electrical conductivity. A study of the electrochemical properties of micrometer-thick LTO film electrodes with the same mesoporous morphology is currently ongoing.

CONCLUSIONS

In summary, we have reported a facile polymer-directed sol—gel route to nanocrystalline $Li_4Ti_5O_{12}$ thin films with a well-defined mesoporous morphology. The data in this work collectively verify that the initially amorphous architectures can be fully crystallized while retaining nanoscale porosity. In addition, the structure and morphology results show that the polymer-templated thin films are homogeneous at both the nanoscale and the microscale. More importantly, however, the data demonstrate that the materials employed here can be produced in phase-pure form.

The present work further establishes the benefits of combining a large-pore mesoporous morphology with nanocrystalline thin films to achieve enhancement in electrochemical properties. Mesoporous LTO thin film electrodes not only can reversibly accommodate significant amounts of lithium ions through a two-phase Faradaic reaction at short charging times but also are able to maintain stable cycling performance at rates as high as 64C. We attribute the enhancement of the lithium ion storage capabilities to the unique morphology of the films and the fact that the electrical conductivity is of the same order as that for bulk nanocrystalline LTO despite both the high density of grain boundaries and large number of solid/air interfaces. Overall, this research shows that mesoporous versions of phase-pure LTO spinel have promise as high rate anode materials for thin film microbatteries and hybrid supercapacitor applications. These results are exciting, considering the trend toward redox-active materials that can be charged within seconds and exhibit long-term cycling stability.

ASSOCIATED CONTENT

Ⓢ Supporting Information. Low-magnification microscope images before and after galvanostatic cycling. High-resolution XPS spectrum of the Li 1s core level region. This material is available free of charge via the Internet at http://pubs.acs.org.

AUTHOR INFORMATION

Corresponding Author

*E-mail: torsten.brezesinski@phys.chemie.uni-giessen.de.

ACKNOWLEDGMENT

This work was supported in part by the Fonds der Chemischen Industrie im Verband der Chemischen Industrie through a Liebig fellowship (T.B.). The authors would like to thank Jan Perlich, Christian Reitz, Anneliese Heilig, Sven O. Steinmueller, Ken-ichi Iimura, Bernd M. Smarsly, and Christoph Weidmann for their assistance in materials preparation and measurements. Portions of this research were carried out at the German synchrotron radiation facility HASYLAB at DESY.

REFERENCES

(1) Conway, B. E. *Electrochemical Supercapacitors*; Kluwer Academic: New York, 1999.

(2) Winter, M.; Brodd, R. J. *Chem. Rev.* **2004**, *104*, 4245–4269.

(3) Bruce, P. G.; Scrosati, B.; Tarascon, J. M. *Angew. Chem., Int. Ed.* **2008**, *47*, 2930–2946.

(4) Whittingham, M. S. *Chem. Rev.* **2004**, *104*, 4271–4301.

(5) Arico, A. S.; Bruce, P.; Scrosati, B.; Tarascon, J. M.; Van Schalkwijk, W. *Nat. Mater.* **2005**, *4*, 366–377.

(6) Jamnik, J.; Maier, J. *Phys. Chem. Chem. Phys.* **2003**, *5*, 5215–5220.

(7) Conway, B. E.; Birss, V.; Wojtowicz, J. *J. Power Sources* **1997**, *66*, 1–14.

(8) Brezesinski, K.; Wang, J.; Haetge, J.; Reitz, C.; Steinmueller, S. O.; Tolbert, S. H.; Smarsly, B. M.; Dunn, B.; Brezesinski, T. *J. Am. Chem. Soc.* **2010**, *132*, 6982–6990.

(9) Riley, L. A.; Cavanagh, A. S.; George, S. M.; Jung, Y. S.; Yan, Y. F.; Lee, S. H.; Dillon, A. C. *ChemPhysChem* **2010**, *11*, 2124–2130.

(10) Winter, M.; Besenhard, J. O.; Spahr, M. E.; Novak, P. *Adv. Mater.* **1998**, *10*, 725–763.

(11) Brezesinski, T.; Wang, J.; Senter, R.; Brezesinski, K.; Dunn, B.; Tolbert, S. H. *ACS Nano* **2010**, *4*, 967–977.

(12) Kim, E.; Son, D.; Kim, T. G.; Cho, J.; Park, B.; Ryu, K. S.; Chang, S. H. *Angew. Chem., Int. Ed.* **2004**, *43*, 5987–5990.

(13) Amatucci, G. G.; Badway, F.; Du Pasquier, A.; Zheng, T. *J. Electrochem. Soc.* **2001**, *148*, A930–A939.

(14) Ferg, E.; Gummow, R. J.; Dekock, A.; Thackeray, M. M. *J. Electrochem. Soc.* **1994**, *141*, L147–L150.

(15) Ohzuku, T.; Ueda, A.; Yamamoto, N. *J. Electrochem. Soc.* **1995**, *142*, 1431–1435.

(16) Mikhailova, D.; Sarapulova, A.; Voss, A.; Thomas, A.; Oswald, S.; Gruner, W.; Trots, D. M.; Bramnik, N. N.; Ehrenberg, H. *Chem. Mater.* **2010**, *22*, 3165–3173.

(17) Prakash, A. S.; Manikandan, P.; Ramesha, K.; Sathiya, M.; Tarascon, J. M.; Shukla, A. K. *Chem. Mater.* **2010**, *22*, 2857–2863.

(18) Allen, J. L.; Jow, T. R.; Wolfenstine, J. *J. Power Sources* **2006**, *159*, 1340–1345.

(19) Armstrong, G.; Armstrong, A. R.; Bruce, P. G.; Reale, P.; Scrosati, B. *Adv. Mater.* **2006**, *18*, 2597–2600.

(20) Pell, W. G.; Conway, B. E. *J. Power Sources* **2004**, *136*, 334–335.

(21) Du Pasquier, A.; Plitz, I.; Menocal, S.; Amatucci, G. *J. Power Sources* **2003**, *115*, 171–178.

(22) Goltner, C. G.; Antonietti, M. *Adv. Mater.* **1997**, *9*, 431–436.

(23) Yang, P. D.; Zhao, D. Y.; Margolese, D. I.; Chmelka, B. F.; Stucky, G. D. *Chem. Mater.* **1999**, *11*, 2813–2826.

(24) Choi, S. Y.; Mamak, M.; Coombs, N.; Chopra, N.; Ozin, G. A. *Adv. Funct. Mater.* **2004**, *14*, 335–344.

(25) Sanchez, C.; Boissiere, C.; Grosso, D.; Laberty, C.; Nicole, L. *Chem. Mater.* **2008**, *20*, 682–737.

(26) Kresge, C. T.; Leonowicz, M. E.; Roth, W. J.; Vartuli, J. C.; Beck, J. S. *Nature* **1992**, *359*, 710–712.

(27) Yang, H.; Kuperman, A.; Coombs, N.; Mamiche-Afara, S.; Ozin, G. A. *Nature* **1996**, *379*, 703–705.

(28) Ciesla, U.; Schuth, F. *Microporous Mesoporous Mater.* **1999**, *27*, 131–149.

(29) Soler-illia, G. J. D.; Sanchez, C.; Lebeau, B.; Patarin, J. *Chem. Rev.* **2002**, *102*, 4093–4138.

(30) Brinker, C. J.; Lu, Y. F.; Sellinger, A.; Fan, H. Y. *Adv. Mater.* **1999**, *11*, 579–585.

(31) Ogawa, M. *Langmuir* **1997**, *13*, 1853–1855.

(32) Li, J.; Jin, Y. L.; Zhang, X. G.; Yang, H. *Solid State Ionics* **2007**, *178*, 1590–1594.

(33) Li, Y.; Pan, G. L.; Liu, J. W.; Gao, X. P. *J. Electrochem. Soc.* **2009**, *156*, A495–A499.

(34) Lu, H. W.; Zeng, W.; Li, Y. S.; Fu, Z. W. *J. Power Sources* **2007**, *164*, 874–879.

(35) Zhu, N.; Liu, W.; Xue, M. Q.; Xie, Z. A.; Zhao, D.; Zhang, M. N.; Chen, J. T.; Cao, T. B. *Electrochim. Acta* **2010**, *55*, 5813–5818.

(36) Thomas, A.; Schlaad, H.; Smarsly, B.; Antonietti, M. *Langmuir* **2003**, *19*, 4455–4459.

(37) Li, D. L.; Zhou, H. S.; Honma, I. *Nat. Mater.* **2004**, *3*, 65–72.

(38) Kuemmel, M.; Grosso, D.; Boissiere, U.; Smarsly, B.; Brezesinski, T.; Albouy, P. A.; Amenitsch, H.; Sanchez, C. *Angew. Chem., Int. Ed.* **2005**, *44*, 4589–4592.

(39) Smarsly, B.; Grosso, D.; Brezesinski, T.; Pinna, N.; Boissiere, C.; Antonietti, M.; Sanchez, C. *Chem. Mater.* **2004**, *16*, 2948–2952.

(40) Kavan, L.; Gratzel, M. *Electrochem. Solid-State Lett.* **2002**, *5*, A39–A42.

(41) Brezesinski, T.; Groenewolt, M.; Pinna, N.; Amenitsch, H.; Antonietti, M.; Smarsly, B. M. *Adv. Mater.* **2006**, *18*, 1827–1831.

(42) Feng, P. Y.; Bu, X. H.; Pine, D. J. *Langmuir* **2000**, *16*, 5304–5310.

(43) Flodstrom, K.; Alfredsson, V. *Microporous Mesoporous Mater.* **2003**, *59*, 167–176.

(44) Leonidov, I. A.; Leonidova, O. N.; Perelyaeva, L. A.; Samigullina, R. F.; Kovyazina, S. A.; Patrakeev, M. V. *Phys. Solid State* **2003**, *45*, 2183–2188.

(45) Chen, C. H.; Vaughey, J. T.; Jansen, A. N.; Dees, D. W.; Kahaian, A. J.; Goacher, T.; Thackeray, M. M. *J. Electrochem. Soc.* **2001**, *148*, A102–A104.

(46) Iwaniak, W.; Fritzsche, J.; Zukalova, M.; Winter, R.; Wilkening, M.; Heitjans, P. *Defect Diffus. Forum* **2009**, *565*, 289–292.

(47) Wilkening, M.; Amade, R.; Iwaniak, W.; Heitjans, P. *Phys. Chem. Chem. Phys.* **2007**, *9*, 1239–1246.

(48) Feitosa, K.; Marze, S.; Saint-Jalmes, A.; Durian, D. J. *J. Phys.: Condens. Matter* **2005**, *17*, 6301–6305.

(49) Peramunage, D.; Abraham, K. M. *J. Electrochem. Soc.* **1998**, *145*, 2609–2615.

(50) Sassoye, C.; Laberty, C.; Le Khanh, H.; Cassaignon, S.; Boissiere, C.; Antonietti, M.; Sanchez, C. *Adv. Funct. Mater.* **2009**, *19*, 1922–1929.

(51) Simon, P.; Gogotsi, Y. *Nat. Mater.* **2008**, *7*, 845–854.